Kinetic Monte Carlo simulation of the elementary electrochemistry in a hydrogen-powered solid oxide fuel cell

Xian Wang [a], Kah Chun Lau [b], C. Heath Turner [a,*], Brett I. Dunlap [c]

[a] *Department of Chemical and Biological Engineering, The University of Alabama, Box 870203, Tuscaloosa, AL 35487-0203, United States*
[b] *Department of Chemistry, George Washington University, Washington, DC 20052, United States*
[c] *Chemistry Division, Code 6189, Naval Research Laboratory, Washington, DC 20375, United States*

ABSTRACT

A hydrogen-powered solid oxide fuel cell (SOFC), with a Pt cathode and a Ni anode, is modeled with a kinetic Monte Carlo (KMC) simulation technique. A series of reversible elementary steps are adopted from experiments and theories for simulating the oxygen reduction reaction near the cathode–electrolyte interface and the hydrogen-oxidation mechanism near the anode–electrolyte interface. By studying the change in the ionic current density, the sensitivity of the kinetic parameters is analyzed, and the influence of various operating conditions and different material properties are also explored. The results show that the dominant elementary process is the oxygen incorporation into the yttria-stabilized zirconia (YSZ) electrolyte at the cathode. Increasing the applied bias voltage, operating temperature, and relative permittivity of the YSZ, but reducing the thickness of the YSZ enhance the ionic current density and improve the efficiency of the SOFC.

© 2010 Elsevier B.V. All rights reserved.

1. Introduction

During the past few decades, solid oxide fuel cells (SOFCs) have attracted increasing interest due to their potential for highly efficient energy conversion, fuel flexibility, and low pollutant emissions [1–3]. Many of the current experimental efforts are focused on improving the operational durability, reducing fuel consumption (i.e., by modifying the chemical composition of the electrode or electrolyte, or by introducing catalytically active intermediate layers) [3–7]. However, in experiments it can be difficult to directly identify the influence of individual electrochemical reactions and mechanisms occurring within these systems; and without this insight, it can be difficult to improve the performance characteristics of SOFCs in a well-defined way.

Recently, in order to complement the on-going experimental progress, various theoretical models, including first-principles approaches and continuum-level theories, have been actively developed. These investigations have contributed toward our understanding of the detailed physical and electrochemical processes in operating SOFCs, especially at the interfacial boundaries of the electrode and the electrolyte [8–12]. For example, ab initio density functional theory (DFT) calculations were per-

formed to study the detailed mechanisms of typical fuel (e.g., H_2 and CH_4) adsorption and oxidation on the yttria-stabilized zirconia (YSZ) surface [13]. The results validated the possibility of the direct oxidation of the fuel without a metallic catalyst on the oxygen-enriched YSZ surface, which is in good agreement with the experimental observations. More recently, DFT calculations have been used to investigate these reactions at the Ni/YSZ/fuel three-phase boundary, with a focus on the fundamental interfacial electrochemistry [14]. Unfortunately, these high-accuracy electronic structure calculations are typically limited to investigations of individual events and small models. Thus, this approach is reasonable for systems with highly localized interactions or highly symmetric geometries [13–16]. On the other hand, several molecular-level and continuum-level methods (such as molecular dynamics simulations, state-space modeling) have been developed in order to model the fluid dynamics, heat balance, and transport phenomena in SOFCs. The previous contributions in the literature have paid more attention to the electrochemical potential balance, the macroscopic current–voltage (*I–V*) relationships, and the continuum-level rate equations of the chemical reactions, but usually neglect the atomic-scale features of the systems [17–20]. Thus, although current theoretical efforts have provided guidance with respect to selecting optimal operating conditions, it is still necessary to develop an atomistic model. It is important that such a model retains enough computational accuracy to deal with the complicated interactions and multiple chemical processes occurring at the elec-

---

trode/electrolyte interfaces, but with a reasonable computational cost.

While there have been modeling analyses ranging from first-principles approaches to macroscale-level models, a single theoretical framework, spanning multiple length scales, is still needed. One possible solution is to use kinetic Monte Carlo (KMC) simulations, since simultaneous atomistic-level events can be captured, even when the events span several orders of magnitude in time and length scales. For instance, Modak and Lusk applied KMC simulations to model the open-circuit voltage and electrical double layer of a doped electrolyte, and then compared their results to a continuum model [21]. In addition, impedance information also has been successfully captured by Pornprasertsuk et al. using KMC calculations [22]. Quite recently, they updated their KMC model to simulate a complete SOFC operating at 900 K, and they investigated two basic electrode geometries (clusters and strips) [23]. Overall, they found that the oxygen adsorption is the slowest step at the cathode and water formation is the slowest step at the anode. While our temperatures are generally higher and our reaction steps are slightly different, we observe similar rate-limiting behavior in our model. All of these previous studies add credibility for using KMC to translate experimental and theoretical rates into an atomistic-level model of a functioning SOFC. Hence, we have focused on further development of the KMC-based approach, with the goal of building a thermodynamically consistent SOFC model, coupled with a realistic (but minimal) set of event details.

In our earlier work, we developed a KMC-based model of the cathode-only side of an SOFC. In the model, we captured the reaction events and electrochemistry associated with the cathode side of an SOFC, along with a sensitivity analysis of the model parameters. In this paper, we present a more comprehensive KMC model, which incorporates both the cathode-side and the anode-side events, relevant to a hydrogen-powered YSZ fuel cell. This is accomplished by adding the surface adsorption/desorption reactions, diffusion, and spillover of fuel gas at the anode. In our original model [24–26], the oxygen reduction reaction (ORR) at the cathode side was qualitatively consistent with experimental findings and previous theoretical predictions, as well as our impedance analysis. Our updated model simultaneously considers the electrochemical reactions at both the cathode and anode sides, which should be more representative of a real SOFC. The change of the ionic current density (J) with respect to different material-independent/dependent parameters and geometrical parameters is explored. Ultimately, the simulation results help clarify the correlated behavior of many simultaneously occurring events, and once understood, this information can be used for bottom-up design of SOFCs.

2. Methodology

Understanding fuel cell operation at microscopic length and time scales (i.e., identifying the reaction pathways, the effect of local electric fields on chemical reactions, oxygen ion and vacancy transfer rates, and chemical interactions at cathode–electrolyte and anode–electrolyte interfaces) is important for determining various boundary conditions in macroscopic studies and for the general design of fuel cells. The model used here represents a minimal depiction of an SOFC device, composed of an ideal YSZ electrolyte, a Pt cathode, and a Ni anode (the details are given in Section 2.1). For this idealized system, the ORR takes place at the three-phase boundary (TPB) on the cathode side, according to the following reaction:

$$(1/2)O_2(gas) + 2e^-(Pt\ cathode) \rightarrow O^{2-}(YSZ\ electrolyte) \qquad (1)$$
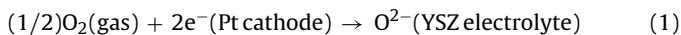
While the reaction at the TPB on the anode side is formulated as:

$$H_2(gas) + O^{2-}(YSZ\ electrolyte) \rightarrow H_2O(gas) + 2e^-(Ni\ anode) \qquad (2)$$
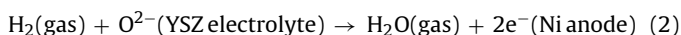
While these pivotal electrochemical reactions can be decomposed into several competing pathways, we assume here that they can be represented by an abbreviated set of well-defined reaction steps. For each of the allowed reaction pathways, the relevant parameters and the molecular intermediates were captured within the framework of KMC simulations. While the catalyst size and gas pressure dependence of the electrode reaction rates have been modeled with KMC in Ref. [23], here, we primarily focused on the predicted ionic current density J (mA cm^{-2}) from our model, as a function of the simulation parameters. These parameters were divided into three general categories: (i) *kinetic parameters*, including the activation barriers (E_a) and the pre-exponential factors (F_0); (ii) *material-independent parameters*, such as the external applied bias voltage (V_{ext}) and the temperature (T); and (iii) *material-dependent parameters*, including the electrolyte thickness (D) and the relative permittivity (ε_r) of the electrolyte. To identify the influence of each of the model parameters in a well-defined manner, we varied each of these parameters independently, while keeping all of the others fixed.

Some aspects of the experimental systems are not included in our model, due to their complexity (e.g., thermally or electrically induced chemical and morphological changes of the electrode/electrolyte interfaces), but we have attempted to capture the primary experimental features. In addition, since we only consider a minimal set of chemical reactions (as compared to the real experimental chemistry), only limited effects at the anode and cathode TPB can be realized in this study.

2.1. Model description

To further simplify our simulation, infinitesimally thin cathode and anode layers were used to model the electrodes (i.e., the real three-dimensional porous structures of the two electrodes were not explicitly modeled). As a consequence, neither the oxygen transport through the porous Pt cathode nor the fuel gas (H_2) transport through the Ni anode was captured. Although our model does not consider the diffusion through the cathode or anode, the main physicochemical reactions occurring at the Pt/YSZ and Ni/YSZ interfaces were still preserved, and the details are listed in Table 1. We consider eight elementary reactions at the cathode (events 1–7 and 9 in Table 1), 14 elementary reactions at the anode (events 10–23 in Table 1), and diffusion of the oxygen vacancies (represented by event 8) within the YSZ electrolyte.

Sandwiched between the Pt cathode and the Ni anode, the 9 mol% YSZ was modeled as a supercell, with a (1 0 0) surface in the z direction and with periodic boundary conditions in the x and y directions. The structure is shown in Fig. 1, which corresponds to a perfect cubic fluorite structure (i.e., a *Fm3m* crystal with a fixed lattice parameter (a) of 5.14 Å [27]). Throughout the simulation,
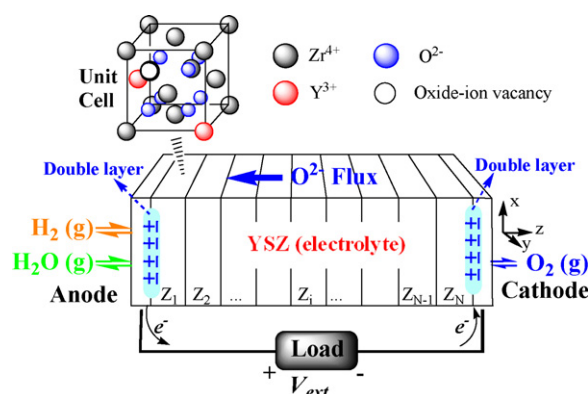

Fig. 1. Illustration of the hydrogen-powered YSZ fuel cell model used in this study.

Table 1
Kinetic parameters [16,17,21,22,25,31–39] used in the KMC simulations, where the θ is the local surface coverage.

Event	Location	Event name	Elementary step	Prefactor F_0	Activation barrier E_a	Reference
1	Cathode	Adsorption k_1	$O_2(g)+(*)\rightarrow O_2{}^*$	$s_0 = 0.18$ (trapping probability)	$m = 14.1$ (sticking exponent)	[17,35]
2	Cathode	Desorption k_2	$O_2{}^*\rightarrow O_2(g)+(*)$	1.0×10^{13} s^{-1}	$37.0-21.0\theta$ kJ mol^{-1}	[17,36]
3	Cathode	Diffusion k_3	$O_2{}^*\rightarrow O_2{}^*$	4.65×10^{-5} m^2 s^{-1}	140.5 kJ mol^{-1}	[17,32,33]
4	Cathode	Dissociation k_4	$O_2{}^*+(*)\rightarrow O^-{}^*+O^-{}^*$	5.0×10^{11} s^{-1}	$33.0+16\theta$ kJ mol^{-1}	[17,35]
5	Cathode	Dimerization k_5	$O^-{}^*+O^-{}^*\rightarrow O_2{}^*+(*)$	2.4078×10^{14} m^2 s mol^{-1}	$250.0-50\theta$ kJ mol^{-1}	[36,37]
6	Cathode	Diffusion k_6	$O^-{}^*\rightarrow O^-{}^*$	4.65×10^{-5} m^2 s^{-1}	140.5 kJ mol^{-1}	[17,32,33]
7	Cathode	Incorporation k_7	$O^-{}^*+V_{\ddot{o}}+e^-\rightarrow O^{2-}(YSZ)+(*)$	2.7899×10^{10} m^3 s^{-1} mol^{-1}	$130.0+48.2425\theta$ kJ mol^{-1}	[25,17]
8	YSZ	Diffusion k_8	$V_{\ddot{o}}\rightarrow V_{\ddot{o}}$	1.9×10^{13} s^{-1}	101.3 kJ mol^{-1}	[16,21,22,31,17,34]
9	Cathode	Excorporation k_9	$O^{2-}(YSZ)+(*)\rightarrow O^-{}^*+V_{\ddot{o}}+e^-$	2.7899×10^{10} m^3 s^{-1} mol^{-1}	$130.0+48.2425\theta$ kJ mol^{-1}	[25,17]
10	Anode	Adsorption k_{10}	$H_2(g)+2(*)\rightarrow H^*+H^*$	$\zeta = 0.01$ (trapping coefficient)	–	[38]
11	Anode	Formation k_{11}	$O^-{}^*+H^*\rightarrow OH^-{}^*$	1.0×10^{13} s^{-1}	97.9 kJ mol^{-1}	[39]
12	Anode	Dissociation k_{12}	$OH^-{}^*\rightarrow O^-{}^*+H^*$	5.213×10^{12} s^{-1}	37.19 kJ mol^{-1}	[39]
13	Anode	Association k_{13}	$H^*+H^*\rightarrow H_2(g)+2(*)$	1.45418×10^{11} s^{-1}	88.12 kJ mol^{-1}	[39]
14	Anode	Formation k_{14}	$OH^-{}^*+H^*\rightarrow H_2O^*$	7.8×10^{11} s^{-1}	42.7 kJ mol^{-1}	[39]
15	Anode	Desorption k_{15}	$H_2O^*\rightarrow H_2O(g)+(*)$	4.579×10^{12} s^{-1}	62.68 kJ mol^{-1}	[39]
16	Anode	Adsorption k_{16}	$H_2O(g)+(*)\rightarrow H_2O^*$	$\zeta = 0.1$ (trapping coefficient)	–	[38]
17	Anode	Excorporation k_{17}	$O^{2-}(YSZ)+(*)\rightarrow O^-{}^*+V_{\ddot{o}}+e^-$	2.7899×10^{10} m^3 s^{-1} mol^{-1}	$130.0+48.2425\theta$ kJ mol^{-1}	[25,17]
18	Anode	Incorporation k_{18}	$O^-{}^*+V_{\ddot{o}}+e^-\rightarrow O^{2-}(YSZ)+(*)$	2.7899×10^{10} m^3 s^{-1} mol^{-1}	$130.0+48.2425\theta$ kJ mol^{-1}	[25,17]
19	Anode	Diffusion k_{19}	$H^*\rightarrow H^*$	4.65×10^{-5} m^2 s^{-1}	140.5 kJ mol^{-1}	[17,32,33]
20	Anode	Diffusion k_{20}	$OH^-{}^*\rightarrow OH^-{}^*$	4.65×10^{-5} m^2 s^{-1}	140.5 kJ mol^{-1}	[17,32,33]
21	Anode	Diffusion k_{21}	$H_2O^*\rightarrow H_2O^*$	6.6×10^{-9} m^2 s^{-1}	140.5 kJ mol^{-1}	[17,32,33,38]
22	Anode	Dissociation k_{22}	$H_2O^*+(*)\rightarrow OH^-{}^*+H^*$	5.655×10^{12} s^{-1}	91.36 kJ mol^{-1}	[39]
23	Anode	Diffusion k_{23}	$O^-{}^*\rightarrow O^-{}^*$	4.65×10^{-5} m^2 s^{-1}	140.5 kJ mol^{-1}	[17,32,33]

all of the Y'_{Zr} and Zr ions are in a fixed position, while the oxygen ion vacancies are allowed to migrate, consistent with experimental findings [27]. Consistent with our previous work [24], an external applied bias voltage V_{ext} was applied to our system. According to our model, V_{ext} corresponds to the voltage drop between the electrodes across the YSZ electrolyte. Consistent with the concentration of gases at the anode and cathode, we assume that the voltage drop in our model can vary from 0 to -1.2 V. In the absence of this driving force, the net current is zero. Once the simulation begins, and the voltage drop is introduced, the ions begin flowing from the cathode side toward the anode side. Therefore, the ionic current density is obtained by calculating the net flux of oxygen ions (O^{2-}) passing through the YSZ (100) surface per unit time, divided by the cross-sectional area of the electrolyte. Following our previous work [24–26] and the suggestion from Ref. [17], we defined the TPB region at each electrode/YSZ interface to correspond to a fractional surface area of 0.01 (the width and length of the TPB region were assumed to be 10 nm and 100 m, respectively, per 1 cm^2 area of the porous electrode). Thus, our final reported values of the simulated ionic current density (J) have been *scaled*, proportional to this experimentally based value. To emphasize this fact, we refer to the ionic current as "scaled ionic current" throughout this work. Furthermore, we neglected explicit treatment of the electrons which, according to the Born–Oppenheimer approximation, were assumed to move much faster onto and through the electrodes than the movement of the ions [17].

As shown in Fig. 1, the cubic YSZ electrolyte was represented as a series of parallel plate capacitors Z_i, where every Z_i plane includes a (100) cation plane and a (100) anion plane, with a spacing of $0.5a$ within the (100) plane of the cubic fluorite lattice [22,24]. In our model, the corresponding three-dimensional Poisson equation of electrostatics is approximated as a one-dimensional system, by assuming that the charge within each plane is evenly distributed and unaffected by ionic translations in the x and y directions [28,29]. Based on this approximation, the KMC simulation time is significantly reduced, since our procedure requires that the local charge distribution be updated after each step.

2.2. Kinetic parameters

As mentioned in the previous section, the basic electrochemistry within the cathode, anode, and electrolyte of our SOFC model can be represented by 23 distinct electrochemical reactions (Table 1). These events are designed so that each forward event has a corresponding reverse event (i.e., adsorption/desorption, forward/reverse reaction). According to harmonic transition state theory [30], all the state-to-state dynamics and reaction paths can be approximated by a series of well-defined rate constants. Hence, we introduced 46 kinetic parameters (which come from experimental measurements or high-level theoretical calculations in the literature) [16,17,21,22,25,31–39] as activation barriers or pre-exponential factors for defining the event rates.

As suggested by Mitterdorfer and Gauckler [17] the adsorption rate constants of O_2, H_2, and H_2O (i.e., k_1, k_{10}, k_{16}) were approximated by their flux rate (F_{gas}) taken from the kinetic theory of gases, along with a coverage-dependent sticking coefficient (ζ_{gas}).

$$k_{ads}[gas] = \zeta_{gas}\times F_{gas} = \zeta_{gas}\frac{N_A P_{gas}}{\sqrt{2\pi MRT}} \tag{3}$$

Here, N_A is Avogadro's number, R is the gas constant, T is the absolute temperature, M is the molecular weight, and P_{gas} is the gas partial pressure of O_2, H_2, or H_2O. The sticking coefficient of hydrogen and water are taken directly from Ref. [38]. However, following an experimental study [35], the sticking coefficient of oxygen includes a coverage-dependent term. In this case, the sticking coefficient is calculated by an approximation of the surface trapping probability s_0, the sticking exponent m, and the local surface coverage θ (at the cathode side), as expressed by the following equation:

$$\zeta_{gas,\,oxygen} = s_0\,\exp(-m\theta) \tag{4}$$

As in our previous KMC simulations [24–26], the oxygen surface coverage is calculated *locally*. In this way, the adsorption rate at a particular site depends upon the local coverage (nearest-neighbors).

The rates corresponding to desorption, diffusion, dissociation, and association reactions (i.e., k_2–k_6, k_8, k_{11}–k_{15}, and k_{19}–k_{23}) are expressed in an Arrhenius form. The rate expressions include an activation barrier (E_a), a pre-exponential factor (F_0), and sometimes a coverage-dependent correction to the reaction rate:

$$k_i = F_{0i}\,\exp\left(-\frac{E_{ai}}{k_B T}\right) \quad (i = 2\text{–}6,\ 8,\ 11\text{–}15,\ \text{or}\ 19\text{–}23) \tag{5}$$

where k_B is Boltzmann's constant and the subscript i denotes the event number.

The final four events (k_7, k_9, k_{17}, and k_{18}) correspond to the charge transfer into and out of the YSZ, as oxygen ions are incorporated into (at the cathode) or expelled from (at the anode) the electrolyte. The general rate expression for these events is given by Mitterdorfer and Gauckler [17] as:

$$k_i = k_i' \exp(b'E) \quad (i = 7, 9, 17, \text{ or } 18) \tag{6}$$

When $i = 7$ and 18, b' is expressed as $b' = -\beta F/RT$; while, when $i = 9$ and 17, $b' = -(1-\beta)F/RT$, where F is Faraday's constant, E is the applied potential, and β is charge-transfer coefficient. In addition, the k_i' term is expressed by an Arrhenius form, with a corresponding activation barrier (E_a) and pre-exponential factor (F_0):

$$k_i' = F_{0i} \exp\left(-\frac{E_{ai}}{RT}\right) \quad (i = 7, 9, 17 \text{ or } 18) \tag{7}$$

Eq. (6) indicates that these four events are significantly affected by the voltage drop across the electrode/YSZ interface. Hence, as the applied voltage is varied, the migration of ions (i.e., the current) through the YSZ is controlled.

2.3. Kinetic Monte Carlo (KMC) modeling

In KMC modeling, the system is propagated through time, by stochastically selecting the next event to occur, depending upon the relative probability of each possible event in the system [40]. The relative probability of each event is generally dictated by the intrinsic rate constant of each event, which must be defined a priori in the simulation (i.e., Table 1). The probability of each event is affected by the local environment, and therefore, must be updated at each step. As the system is propagated, we increment the simulation clock, which approximates the real physical time elapsed.

Once the kinetic database was assembled and the initial configuration of the YSZ structure was generated, the simulation was executed in the following way. According to the dopant fraction (here, 9 mol% of Y_2O_3), the lattice contained a certain fraction of vacancies ($V_{\ddot{o}}$) and a corresponding stoichiometric fraction of yttrium (Y) species, which were distributed randomly throughout the YSZ structure. All of the surface adsorption sites at the cathode and anode sides were initially empty. On the cathode side, the adsorption sites are the locations that can accommodate either an O_2 molecule or an oxygen atom. On the anode side, the adsorption sites can accommodate hydrogen atoms, oxygen atoms, hydroxyl groups, or water molecules. Once the initial configuration was determined, the rate of each event that might potentially occur at each site was tabulated. Our lattice model accelerates this calculation, since the event rates at each lattice site can be quickly determined, without having to calculate nearest-neighbor distances.

After obtaining the rate of each event i for atom number j of atom type k at each site (x, y, z), the total rate of each event for all sites, rate(i) can be calculated by Eq. (8), as well as the total rate of all events (rate$_{total}$), as shown in Eq. (9).

$$\text{rate}(i) = \sum_{j=1}^{N_k} \sum_{k=1}^{N_{types}} \text{rate}_{event}(i, j, k) \tag{8}$$

$$\text{rate}_{total} = \sum_{i=1}^{N_{events}} \text{rate}(i) \tag{9}$$

Once the initial system configuration is generated and rates are calculated, a specific event is chosen to occur according to the relative probability of each event (P_{event}):

$$P_{event}(i, j, k) = \frac{\text{rate}_{event}(i, j, k)}{\text{rate}_{total}} \tag{10}$$

Then, a random number (RN) between 0 and 1 is generated in order to increment the system clock by Δt:

$$\Delta t = -\frac{\ln(RN)}{\text{rate}_{total}} \tag{11}$$

According to the KMC simulation scheme, there is a 100% probability of event acceptance, once the event is chosen. Subsequently, an updated system configuration leads to updated values of rate$_{event}$, rate(i), and rate$_{total}$. Once these event rates are updated, the KMC procedure is repeated (many times) until a predefined number of simulation steps is reached.

2.4. Sensitivity analysis

In our model, the complex electrochemical reactions were simulated by many predefined simulation parameters, which were extracted from several different references in the literature. Therefore, a sensitivity analysis was used to extract and interpret the complex interdependences of these parameters on a target quantity, i.e., the current density. As suggested by Bessler [41] the sensitivity S can be calculated by simulating a target quantity Φ (e.g., the ionic current density) with respect to a small change in one of the model kinetic parameters q (e.g., an activation barrier E_{ai} or a pre-exponential factor F_{0i}) from its initial value.

$$S = \frac{\Delta \Phi}{\Delta q} \tag{12}$$

By assuming each model kinetic parameter q_i as a single independent variable, the complex non-linear dependence of our model kinetic parameters can therefore be extracted and analyzed. Our previous study [25] established that a variable range of $q_i \pm 25\% q_i$ was sufficient to estimate the sensitivity of the ionic current density with respect to each parameter. Thus, we again chose a range of parameter variability of $\pm 25\%$, while the other parameters were held fixed.

3. Results and discussion

In our previous papers [24,25], we established a KMC-based model for the cathode side of an SOFC, and we performed a systematic sensitivity analysis of the kinetic parameters. In this paper, we report our modeling results of the same properties (including sensitivity analysis and the change of scaled ionic current density) with a more comprehensive SOFC model, which now includes the anode-side reactions.

As a reference for our study, a set of parameters is chosen to define a standard baseline simulation system. The parameters are divided into three groups and their baseline values are: (i) kinetic parameters of the electrochemical reactions, as shown in Table 1; (ii) material-independent parameters, with temperature $T = 1073$ K, external applied bias voltage $V_{ext} = -1.0$ V (negative applied voltages at the cathode and zero voltage at the anode), and gas partial pressures of $P_{O_2} = 0.30$ atm (consistent with our previous study [24]), $P_{H_2} = 0.98$ atm, and $P_{H_2O} = 0.02$ atm, with the proportion of H_2 and H_2O suggested by an experimental study [42]; and (iii) material-dependent parameters, with cross-sectional area $A = (10a)^2 = 26.42$ nm^2, thickness of the YSZ $D = 80a = 41.12$ nm, relative permittivity of the YSZ $\varepsilon_r = 40$, and a vacancy concentration corresponding to 9 mol% yttria-doped zirconia. The simulated ionic current density in the standard simulation system was used to gauge the sensitivity of the system to changes in the model parameters.
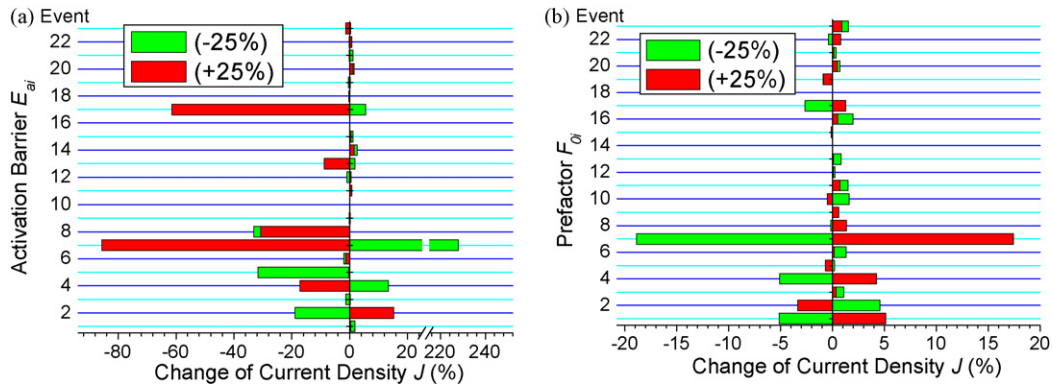
Fig. 2. Sensitivity analysis of the ionic current density J with respect to various kinetic parameters: (a) activation barrier E_a and (b) pre-exponential factor F_0 for events 1–23, as shown in Table 1.

3.1. Analysis of kinetic parameters

The results of the sensitivity analysis with respect to the kinetic parameters are shown in Fig. 2. In this graph, the bars indicate the change of current density when an activation barrier or a pre-exponential factor increases or decreases by 25%. Comparing the sizes of bars in Fig. 2a and b, it is clear that the ionic current density is generally more sensitive to the changes of the activation barriers than by the changes of the pre-exponential factors, as expected.

The largest bar corresponds to the most influential parameter (i.e., event 7), which corresponds to the oxide ion transfer into the cathodic TPB region of the YSZ. Next, the excorporation of O^{2-} from the YSZ to the anode surface as O^{-*} (event 17) is the second most sensitive reaction for the ionic current density. Since both events 7 and 17 are directly related to the flux of the oxygen ions flowing through the electrolyte, these event rates have a strong influence on the simulated current density. Similarly, the current density is also remarkably sensitive to the activation barrier (ΔE_{a8}) of the oxygen vacancy ($V_{\ddot{o}}$) migration within the YSZ (event 8), since this event dictates the ionic transfer rate within the electrolyte.

Additionally, there are minor changes in J with respect to several of the activation barriers. These weaker dependencies correspond to the dissociation of O_2^* into two O^{-*} (ΔE_{a5}) and its inverse reaction (ΔE_{a4}), as well as the desorption of O_2^* (ΔE_{a2}). This suggests that the number of oxygen species occupying the cathode/YSZ interface does not play a major limiting role in the ionic transport, considering the overall performance of the SOFC.

Changing other kinetic parameters only leads to very small deviations in the current density (e.g., $\Delta J < 5\%$). Many of these weak influences correspond to the kinetic parameters of the hydrogen reactions. Thus, the small bars in Fig. 2 suggest that the adsorption reactions of gas molecules (including O_2, H_2, and H_2O) at the cathode or anode surface, the diffusion of molecules or ions along the TPB region, and the formation or dissociation of OH^- and H_2O are not significant determinants of the ionic current. This is good *a posteriori* justification for some of the approximated activation barriers and pre-exponential factor in Table 1 for many of the surface diffusion reaction steps (e.g., the diffusion of H^*, OH^{-*}, O^{-*}, etc.).

To summarize, the most sensitive rates for predicting the current are O^{2-} incorporation at the cathode side, its excorporation at the anode side, as well as the oxygen vacancy diffusion within the YSZ bulk, which also affects the net charge distribution within our simulation cell. These results are in good agreement with our previous study [25], although it only modeled a half-cell (the cathode side). Similar findings indicate that most of the reactions on the anode side play less significant roles in the overall SOFC performance.

With respect to the mobile charge carriers, the charge accumulation happens at the interface of the electrode/electrolyte, which significantly modifies the intrinsic properties of these interfaces. More specifically, the mobile positive charge carriers $V_{\ddot{o}}$ (shown in Fig. 3a) accumulate near a negatively charged cathode and deplete near a positively charged anode. On the contrary, as shown in Fig. 3b, the negative O^{2-} ions display the opposite behavior (i.e., accumulate at the anode side and deplete at the cathode side) to maintain charge neutrality within the YSZ bulk. Therefore, following the Gouy–Chapman model [43], electric double layers, which have large electrochemical capacitances, are formed at the cathode/YSZ and anode/YSZ interfaces. If the activation barrier E_{a7} is decreased (e.g., reduced by 25%), neither the oxygen ions nor the oxygen vacancies stay long enough to accumulate at the TPB region, due to the rapid exchange with the electrolyte. Hence, the corresponding double layers are reduced, as shown by the solid line in Fig. 3. As mentioned in Ref. [23], the concentration of vacancies in the double layer determines the overpotential, which in turn, controls the charge-transfer flux. Thus, with E_{a7} reduced, the current density increases rapidly (e.g., J increases about 228% with a 25% reduction of E_{a7}), partially due to the small polarization and charge-transfer resistances in the TPB regions. These findings suggest that understanding the oxide ion incorporation mechanism at the cathode/electrolyte interface is critical for obtaining high
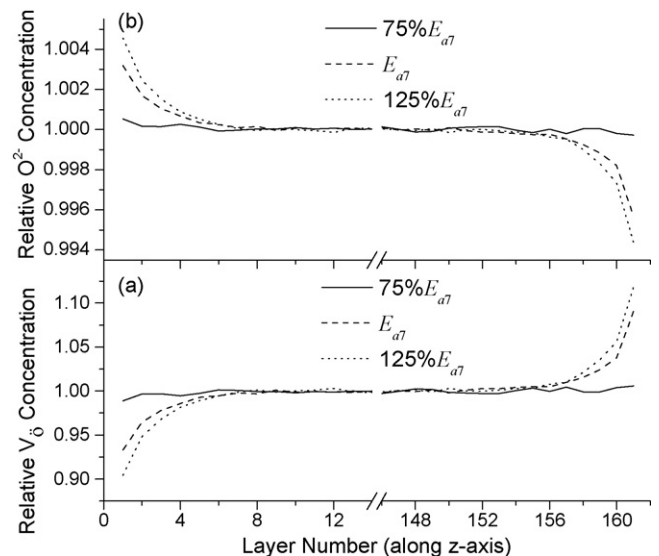
Fig. 3. The relative concentrations of (a) $V_{\ddot{o}}$ and (b) O^{2-} within the YSZ layers corresponding to different values of the activation barrier E_{a7} (i.e., $75\%E_{a7}$, E_{a7} and $125\%E_{a7}$).
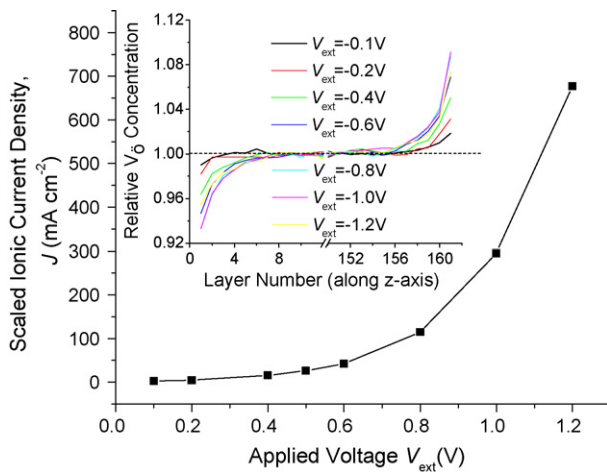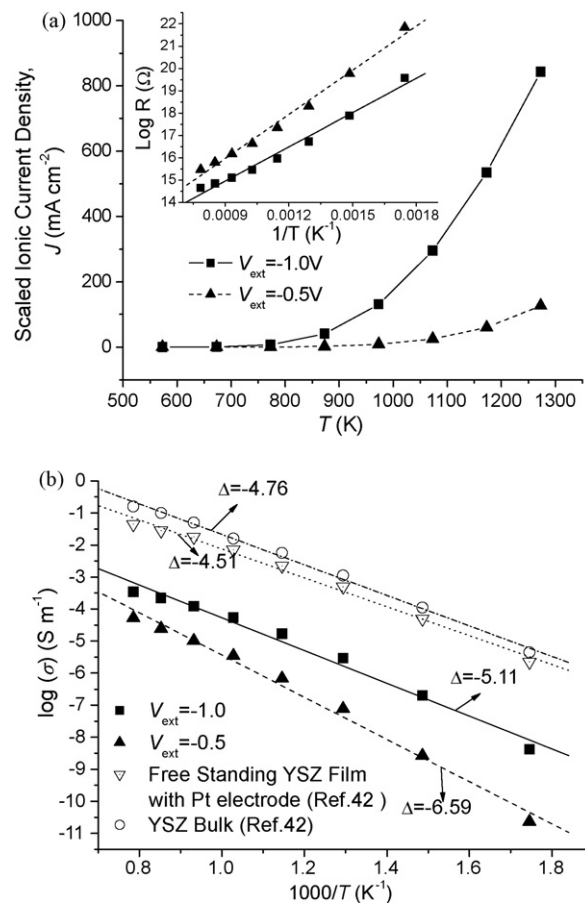
Fig. 4. The scaled ionic current density J (mA cm^{-2}) versus the external applied potential V_{ext} (all are negative applied voltages at the cathode) at T = 1073. The inset shows the relative $V_{\ddot{o}}$ concentrations of the YSZ layers as the function of the external applied potential V_{ext}.

current densities, and for the design and optimization of effective cathode interface structures of future SOFC materials.

3.2. Analysis of material-independent parameters

Besides the influence of the fundamental kinetic parameters describing the system events, the thermodynamic operation variables have an important impact on the simulated ionic current density. Here, the external applied bias voltage V_{ext} and the temperature T are investigated, since our previous study [24,26] of the cathode half-cell showed a great deal of sensitivity to these operational variables, as do experiments.

For a given fuel cell system, the current density is dominated by the reactant concentration and the overpotential losses at the interface of the electrode/electrolyte, as suggested by the Butler–Volmer equation [44]. Thus, the magnitude of J can be studied as a function of the external bias voltage between the cathode and anode, while keeping the gas partial pressures constant $P_{O_2} : P_{H_2} : P_{H_2O} = 0.3 : 0.98 : 0.02$, and fixing the other thermodynamic parameters of the standard simulation system. According to Nernst equation, the standard hydrogen–oxygen electrode potential, or Gibbs free energy of hydrogen and oxygen reacting to give liquid water, is 1.23 V, so the open-circuit voltage for our model should be smaller than this value under normal operating conditions. Here, we varied the external applied bias voltage from 0.1 V to 1.2 V, and the model results are displayed in Fig. 4. The scaled ionic current density increases with applied voltage, with increasing slope at higher V_{ext} values. In the model a non-ohmic I–V curve is present above 0.2 V, while an ohmic I–V curve is found at V_{ext} <0.2 V. If the applied voltage is decreased to zero, there is no net flow of oxygen ions through the YSZ electrolyte, which means that the calculated value of J is zero. In this case, only random fluctuation of O^{2-} and $V_{\ddot{o}}$ concentrations are found throughout the YSZ layers. Thus, a net flow of ionic current is only possible when the external applied voltage allows the random motion of ions such as O^{2-} and $V_{\ddot{o}}$ to flow in the appropriate direction. As shown in the inset of Fig. 4, when the external bias voltage is applied, the oxygen vacancies prefer to deviate from their initial uniform distribution and accumulate at the cathode side, which results in a space-charge region (i.e., double layer). At the same time, the oxygen ions accumulate at the anode side, leading to a similar double-layer structure near the anode/YSZ interface. As the external applied voltage increases, the charge accumulation at each interface becomes more significant,

Fig. 5. (a) The scaled ionic current density as a function of temperature at different V_{ext}. The corresponding simulated resistances of the $10 \times 10 \times 80$ YSZ supercells are displayed in the inset. (b) The simulated conductivity compared to the experiment [42] (in log(σ)) as a function of inverse temperature (in 1000/T).

which modifies the local potential gradients, and the calculated current density J.

In order to investigate the effects of temperature, we computed the ionic current density at temperatures ranging from 573 K to 1273 K, which contains the range of experimental interest. From Fig. 5a, we find that at two different applied voltages ($V_{ext} = -1.0$ V and -0.5 V), the scaled ionic current density grows remarkably with respect to temperature. This tendency is magnified when the applied voltage is large. Moreover, the higher temperatures weaken the polarization resistance due to the accelerated ion migration and chemical reaction kinetics. On the contrary, at low temperature (e.g., T < 700 K), the scaled ionic current density is close to zero. This highlights one of the main challenges of an SOFC operation. Namely, lower temperatures (T < 800 °C) are desired for minimizing material costs, but the performance characteristics decrease at lower temperatures.

The change of conductivity of YSZ (σ) with respect to temperature has been summarized in Fig. 5b, where the conductivity of YSZ (σ) is calculated as:

$$\sigma = \frac{D}{RA} = \frac{ID}{V_{ext}A} = \frac{JD}{V_{ext}} \quad (13)$$

where R is the resistance. In Fig. 5b, the experimentally measured conductivity of a free-standing YSZ film (with a thickness of 30 μm) with Pt electrodes (open triangles) is shown, along with the conductivity of bulk YSZ (open circles). As seen, the Pt/YSZ system displays lower conductivity, most likely due to incomplete contact at the experimental Pt/YSZ interface [42]. Our simulation results,
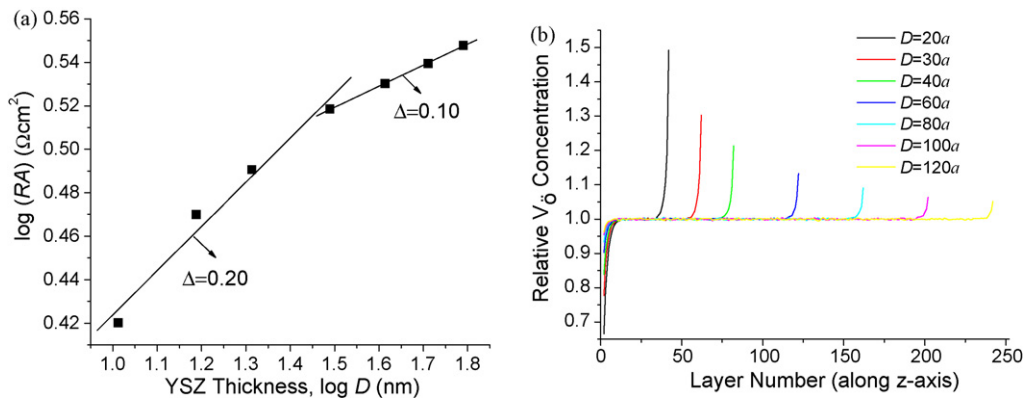
Fig. 6. (a) The logarithmic plot of resistance RA ($\Omega\,cm^2$) versus logarithmic plot of YSZ thickness D (in nm) of the YSZ. (b) The relative $V_{\ddot{o}}$ concentrations of the YSZ layers as the function of the thickness D.

especially at $V_{ext} = -1.0\,V$ (closed squares), are in good qualitative agreement with the experiments. As a function of temperature, our simulated conductivity shows a trend that is very similar to the experimental observation. Deviations from the experimental results may be traced back to the differences between the theoretical model and experimental operating conditions, such as the thickness of the electrolyte and the electrode material. In our model, the thickness of YSZ is only 41.12 nm and the anode is ultra-thin metal Ni. In addition, some of the limitations and assumptions inherent to our model (i.e., neglect of the electrode structure or true TPB regions, etc.) are other elements which lead to the deviations between the theoretical simulations and the experimental measurements.

Assuming an Arrhenius temperature dependence, the corresponding electrolyte YSZ effective resistance can be extracted, as shown in the inset of Fig. 5a. Furthermore, by fitting to an Arrhenius model, the effective activation energy (E_{act}) of the system can be obtained via the following equation:

$$E_{act} = 2.3026 \times k_B \times slope \left(\log R \, vs. \, \frac{1}{T} \right) \tag{14}$$

where k_B is Boltzmann's constant. According to Eq. (14), the effective activation energy of the oxide ion diffusion for the 9 mol% YSZ in our model is estimated to be 1.01 eV and 1.31 eV, corresponding to the applied bias voltage is $-1.0\,V$ and $-0.5\,V$, respectively. These values compare favorably to the experimentally reported values (ranging from 0.83 eV to 1.05 eV) [22,34].

3.3. Analysis of material-dependent parameters

As mentioned above, decreasing the operating temperature degrades the electrolyte ionic conductivity significantly. Thus, at low operation temperatures, two possible routes for enhancing the SOFC performance are improving the electrode/electrolyte structure or developing new electrolyte materials. Therefore, it is valuable to explore the influence of these material-dependent parameters in our model, as described in the following sections.

Since the contributions of the metal electrodes at the YSZ surfaces are not explicitly considered within our model, a bulk-like conductivity (e.g., a single YSZ crystal) is not sensitive to the variation of the surface/interface cross section [24]. Over a range of cross sections (from 32 nm^2 to 117 nm^2), the variation of the calculated ionic current density in our previous modeling study was found to be less than 1% at a temperature 1073 K [24]. This is consistent with the fact that our calculated values of J are reported on a normalized basis (ionic flux/area). Therefore, in this study, we only investigate the influence of the YSZ thickness D (from 20a to 120a) at a fixed cross-sectional area $A = (10a)^2$. The fluctuation of the ionic current density due to the variation of the YSZ thickness D is substantial. The thickness controls the length of diffusive ionic scattering in the region of the potential drop between the anode and cathode. As shown in Fig. 6a, the logarithmic (RA) is plotted as a function of the logarithmic thickness D, where the slopes coming from linear regression fitting are 0.20 (i.e., $RA \propto D^{0.20}$) at $D = \sim 20a$–$60a$ and 0.10 (i.e., $RA \propto D^{0.10}$) at $D = \sim 60a$–$120a$. Thus, although the ionic resistance of the YSZ is found to be dominated by lattice controlled diffusivity, the resistance attributed to the ionic diffusion within the YSZ lattices does not strictly follow Ohm's law of a classical conductor (i.e., $R \propto D$). Furthermore, as the thickness increases, the magnitude of the double layer tends to decrease. As shown in Fig. 6b, the relative $V_{\ddot{o}}$ concentration near the cathode size may increase as much as $\sim$50% from a uniform distribution, when the YSZ thickness is only 20a (i.e., 10.28 nm). However, in the case of a thicker YSZ (e.g., $D = 120a = 61.68$ nm), the increment of $V_{\ddot{o}}$ accumu-
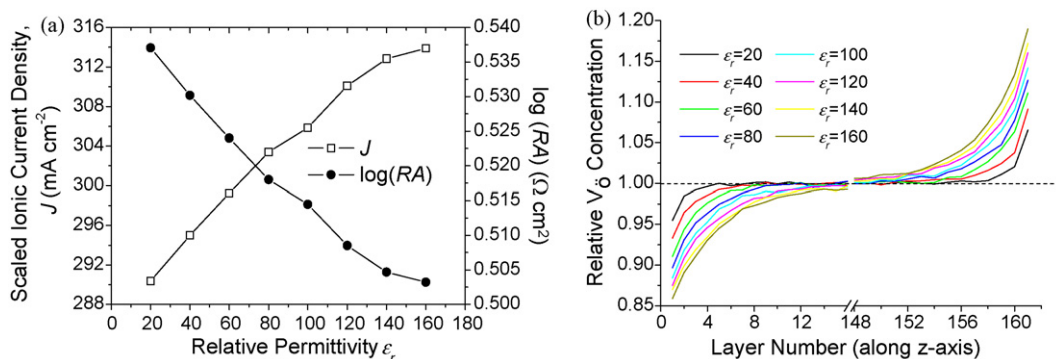
Fig. 7. (a) The scaled ionic current density J (mA cm^{-2}), the logarithmic resistance RA (Ωcm^2) and (b) the relative $V_{\ddot{o}}$ concentrations of the YSZ layers as the function of the effective relative permittivity ε_r.

lation is only ∼5%, relative to the equilibrium value. These results indicate that the effective dielectric capacitance within the double-layer region is inversely proportional to the electrolyte thickness. Therefore, reducing the electrolyte thickness (to a certain extent) can be used to maximize the ionic conductivity in the design of the SOFC.

Local-density-functional response calculations show that YSZ is an electronic insulator with a range of possible dielectric constants, depending on its crystal structure and yttria concentration [45]. The redistribution of mobile ionic species at the electrodes of the YSZ electrolyte upon fuel cell operation (creation of the electrochemical double layers) makes it an effective capacitor. Capacitance is proportional to relative permittivity, ε_r. So instead of fixing the relative permittivity (at $\varepsilon_r = 40$), a series of calculations over a range of ε_r values (from 20 to 160) were performed to predict the effects on the current density J and the effective resistance R of varying permittivity. Fig. 7a shows that the scaled ionic current density is directly proportional to the relative permittivity, while the effective resistance is approximately inversely proportional to the relative permittivity. However, in comparison to the effects of the operating temperature, the response to a similar proportional change of ε_r is not as big. As ε_r increases, there is a larger space-charge polarization at each electrode/electrolyte interface, leading to two obvious electric double layers at the electrode/electrolyte interfaces. These results are similar but extend our previous results [24] for the ORR at the cathode to the full cell. Of all the material-independent parameters, V_{ext} and T have the largest effect on the SOFC current.

4. Conclusions

A hydrogen-powered SOFC is studied by a kinetic Monte Carlo (KMC) model. Its electrolyte, cathode, and anode are 9 mol% YSZ, ultrathin metal Pt, and ultrathin metal Ni, respectively. A series of reversible elementary chemical reaction rates are adopted from the experimental and theoretical literature for simulating the ORR near the cathode and hydrogen-oxidation mechanism near the anode. This minimal list of event rates is intended to capture the most important electrochemical interactions at the two TPB regions of a working SOFC. In order to evaluate the efficiency of the SOFC, the ionic current density J is used as a criterion to perform a sensitivity analysis of the kinetic parameters, and to test the SOFC performance at various operating conditions and different material properties. All of the results are generally consistent with the experimental findings and previous theoretical predictions. It should be emphasized that our model is a highly idealized version of an actual experimental SOFC, so the assumptions and inherent limitations of our model must be considered when making direct comparisons with experimental systems.

Among the reaction rates that we considered, the dominant elementary processes are oxygen incorporation into the YSZ electrolyte at the cathode side, followed by oxygen ion transfer within the YSZ, and finally excorporation out of the electrolyte at the anode side. The influence of varying the rates of the other elementary steps is much less.

Physical parameters such as the applied bias voltage, operating temperature, thickness of the YSZ, and the relative permittivity of the YSZ are found to significantly affect the calculated ionic current density of the SOFC. Increasing the applied bias voltage, operating temperature, and the relative permittivity of the YSZ, but reducing

the thickness of the YSZ are found to increase the ionic current density and improve the efficiency of the SOFC. In order to reduce the inherent limitations of our SOFC model, future development should consider the 3D structure of the two electrodes and extend the database of the electrochemical reaction rates.

References

[1] National Energy Technology Laboratory, Fuel Cell Handbook, DOE/NETL-2004/1206, seventh ed., 2004.
[2] S.C. Singhal, L. Kendall, High-Temperature Solid Oxide Fuel Cells: Fundamentals, Design and Applications, Elsevier Science, Oxford, 2003.
[3] N.P. Brandon, S. Skinner, B.C.H. Steele, Annu. Rev. Mater. Res. 33 (2003) 183.
[4] T. Nakamura, T. Kobayashi, K. Yashiro, A. Kaimai, T. Otake, K. Sato, J. Mizusaki, T. Kawada, J. Electrochem. Soc. 155 (2008) B563.
[5] R.J. Gorte, J.M. Vohs, Curr. Opin. Colloid Interface Sci. 14 (2009) 236.
[6] J. Garcia-Barriocanal, A. Rivera-Calzada, M. Varela, Z. Sefrioui, M.R. Díaz-Guillén, K.J. Moreno, J.A. Díaz-Guillén, E. Iborra, A.F. Fuentes, S.J. Pennycook, C. Leon, J. Santamaria, ChemPhysChem 10 (2009) 1003.
[7] Z.G. Yang, Int. Mater. Rev. 53 (2008) 39.
[8] J. Fleig, Annu. Rev. Mater. Res. 33 (2003) 361.
[9] D. Bhattacharyya, R. Rengaswamy, Ind. Eng. Chem. Res. 48 (2009) 6068.
[10] S. Kakac, A. Pramuanjaroenkij, X.Y. Zhou, Int. J. Hydrogen Energy 32 (2007) 761.
[11] M. Mogensen, K. Kammer, Annu. Rev. Mater. Res. 33 (2003) 321.
[12] W.G. Bessler, S. Gewies, M. Vogler, Electrochim. Acta 53 (2007) 1782.
[13] M. Shishkin, T. Ziegler, J. Phys. Chem. C 112 (2008) 19662.
[14] M. Shishkin, T. Ziegler, J. Phys. Chem. C 113 (2009) 21667.
[15] J. Mukherjee, S. Linic, J. Electrochem. Soc. 154 (2007) B919.
[16] R. Pornprasertsuk, P. Ramanarayanan, C.B. Musgrave, F.B. Prinz, J. Appl. Phys. 98 (2005) 103513.
[17] A. Mitterdorfer, L.J. Gauckler, Solid State Ionics 120 (1999) 211.
[18] A. Bieberle, L.J. Gauckler, Solid State Ionics 146 (2002) 23.
[19] W.G. Bessler, J. Warnatz, D.G. Goodwin, Solid State Ionics 177 (2007) 3371.
[20] J. Rossmeisl, W.G. Bessler, Solid State Ionics 178 (2008) 1694.
[21] A.U. Modak, M.T. Lusk, Solid State Ionics 176 (2005) 2181.
[22] R. Pornprasertsuk, J. Cheng, H. Huang, F.B. Prinz, Solid State Ionics 178 (2007) 195.
[23] R. Pornprasertsuk, T. Holme, F.B. Prinz, J. Electrochem. Soc. 156 (2009) B1406.
[24] K.C. Lau, C.H. Turner, B.I. Dunlap, Solid State Ionics 179 (2008) 1912.
[25] K.C. Lau, C.H. Turner, B.I. Dunlap, Chem. Phys. Lett. 471 (2009) 326.
[26] X. Wang, K.C. Lau, C.H. Turner, B.I. Dunlap, J. Electrochem. Soc. 157 (2009) B90.
[27] C. Pascual, P. Duran, J. Am. Ceram. Soc. 66 (1983) 23.
[28] E. Spohr, J. Chem. Phys. 107 (1997) 6342.
[29] I.C. Yeh, M.L. Berkowitz, J. Chem. Phys. 111 (1999) 3155.
[30] P. Hänggi, P. Talkner, M. Borkovec, Rev. Mod. Phys. 62 (1990) 251.
[31] R. Krishnamurthy, Y.G. Yoon, D.J. Srolovitz, R. Car, J. Am. Ceram. Soc. 87 (2004) 1821.
[32] M.J. Verkerk, A.J. Burggraaf, J. Electrochem. Soc. 130 (1983) 78.
[33] R. Lewis, R. Gomer, Surf. Sci. 12 (1968) 157.
[34] A.I. Ioffe, D.S. Rutman, S.V. Karpachov, Electrochim. Acta 23 (1978) 141.
[35] H.P. Bonzel, R. Ku, Surf. Sci. 40 (1977) 85.
[36] J.L. Gland, B.A. Sexton, G.B. Fisher, Surf. Sci. 95 (1980) 587.
[37] C.T. Campbell, G. Ertl, H. Kuipers, J. Segner, Surf. Sci. 107 (1981) 220.
[38] M. Vogler, A. Bieberle-Hütter, L. Gauckler, J. Warnatz, W.G. Bessler, J. Electrochem. Soc. 156 (2009) B663.
[39] E.S. Hecht, G.K. Gupta, H.Y. Zhu, A.M. Dean, R.J. Kee, L. Maier, O. Deutschmann, Appl. Catal. A: Gen. 295 (2005) 40.
[40] D.P. Landau, K. Binder, A Guide to Monte Carlo Simulations in Statistical Physics, second ed., Cambridge University Press, Cambridge, United Kingdom, 2005.
[41] W.G. Bessler, Solid State Ionics 176 (2005) 997.
[42] O.H. Kwon, G.M. Choi, Solid State Ionics 177 (2006) 3057.
[43] A.J. Bard, L.R. Faulkner, Electrochemical Methods: Fundamentals and Applications, Wiley, New York, 1980.
[44] J. Maier, Physical Chemistry of Ionic Materials: Ions and Electrons in Solids, Wiley, England, 2004.
[45] K.C. Lau, B.I. Dunlap, J. Phys. Condens. Matter 21 (2009) 145402.